Contents lists available at ScienceDirect

Vacuum

Thermal stability of nanocrystalline surface layer of AISI 321 stainless steel

Sadegh Pour-Ali [a], Ali-Reza Kiani-Rashid [a, *], Abolfazl Babakhani [a], Sannakaisa Virtanen [b]

[a] Materials and Metallurgical Engineering Department, Faculty of Engineering, Ferdowsi University of Mashhad, 91775-1111 Mashhad, Iran
[b] Department of Materials Science, WW4-LKO, University of Erlangen-Nuremberg, Martensstrasse 7, D-91058 Erlangen, Germany

ABSTRACT

A nanocrystalline layer with an average grain size of 75 nm was formed on the top surface layer of 321 stainless steel (321SS) alloy via severe shot peening (SSP). Grazing incidence X-ray diffraction (GI-XRD) and transmission electron microscopy (TEM) were applied to characterize the grain size changes, phase compositions and microstructure evolution after vacuum annealing at temperatures ranging from 200 °C to 1000 °C. The results revealed that nanograins slowly grow to ≈ 411 nm as the temperature increases to 600 °C. Dislocation annihilation is shown to be responsible for the changes in grain size up to 600 °C. However, an abnormal grain growth is observed at annealing temperatures of 800 °C and 1000 °C in which grains grow to ≈ 1267 nm and ≈ 2012 nm, respectively. This abnormal grain growth is attributed to the synergistic effect of dislocation annihilation in grain boundaries and triple points, re-arrangement of dislocations, and formation of middle angle ($13°-17°$) grain boundaries. Transformation of stress induced martensite (α') to austenite (γ) and microhardness evolution in the nanocrystalline top surface layer during annealing are also discussed.

© 2017 Elsevier Ltd. All rights reserved.

1. Introduction

In recent decades, surface nanocrystallization (SNC) of austenitic stainless steels (ASSs) has been recognized as a unique way to achieve extraordinary surface properties, namely, surface reactivity [1,2]. Lin et al. [3] reported that surface nanocrystallization of 321 ASS leads to enhanced diffusion of nitrogen during nitriding at 400 °C and remarkably improves its tribological behavior. Peng et al. [4] claimed that in contrast to microcrystalline 304 ASS, breakaway oxidation does not occur for surface nanocrystallized 304 ASS counterpart after exposure to 700–900 °C in air. Based on their report, this improvement is caused by enhanced diffusion of Cr through grain boundaries (GBs) and formation of a Cr-rich oxide in alloy-atmosphere interface. Wang et al. [5] produced a nanocrystalline surface layer on an ASS and pointed out that due to a larger work function and a higher chemical stability, its high-temperature oxidation resistance at 900 °C is much higher than for the microcrystalline one. Here, one issue must be considered and that is the significant grain growth at mentioned high-temperature reactions (nitriding, oxidation and etc.). Actually, it

can be claimed that there is a considerable difference between the grain size of topmost surface at room temperature (i.e. what has been measured in the mentioned studies) and at high temperatures, so that the observed improvements may be due to the presence of ultrafine and/or fine grains in the topmost surface layer, not nano-sized ones.

As a matter of fact, nano-sized grains or nanocrystallites are inherently unstable due to excess energy stored in the grain boundaries which provide great potential driving force for grain growth [6–8]: doubling the grain size of a nanocrystalline material leads to a ~1000 times larger decrease in GBs area than does doubling a micron-scale grain size [9]. This tendency is significantly intensified at temperatures more than half of the melting point of a given metallic material [10]. Many nanocrystalline materials of interest for both fundamental study and engineering applications are now recognized as substantially out of equilibrium and undergo rapid evolution to coarser structures at high temperatures [11,12]. Such coarsening tendencies impede the use of these materials at elevated temperatures. Hence, the significance of this phenomena in both science and industry led to considerable increased attention on this field of research in recent decades [13–15].

The aim of present study is to expand our previous work [16], i.e. to investigate the microstructure evolution of nanocrystalline top

---

* Corresponding author.
E-mail address: kianirashid@um.ac.ir (A.-R. Kiani-Rashid).

surface layer of 321 ASS during high-temperature annealing. A thick nanocrystalline layer was fabricated on the surface of 321 ASS in our previous work via severe shot peening (SSP) [16]. However, the thermal stability of the nanocrystalline surface layer of 321 ASS has not been thoroughly discussed, preventing further application of nanocrystalline 321 ASS at elevated temperatures (as high as 1000 °C). To assess its thermal stability, severe shot peened 321 ASS samples with an average surface grain size of 75 nm were annealed in a wide range of temperature (200 °C–1000 °C). Grazing incidence X-ray diffraction (GI-XRD) and transmission electron microscopy (TEM) were applied to examine the microstructural evolution. In addition, microhardness changes after high-temperature annealing are discussed.

2. Material and methods

The investigated material was 321 ASS, provided by STOOSS company (Switzerland) as 80 mm-diameter bars. The chemical composition of the material was determined by vacuum spark emission spectrometer and is given in Table 1. The bar was solution treated in the argon atmosphere at 1100 °C for 2 h and then rapidly quenched. Cylindrical specimens of 6.0 mm thickness were sectioned from the bar and subjected to SSP (KPS SHOT Co.). SSP with 1000% surface coverage was carried out by a flow of high carbon steel balls with a nominal diameter of 0.5842 mm (S230) and hardness of 45–50 HRC. To generate reproducible plastic strains, the shot angle and the distance between the nozzle and the top surface were set to 90° and 400 mm, respectively. Afterwards, these samples were ultrasonically cleaned in ethanol and dried with hot air. In order to examine the microstructural stability of the nanocrystalline surface layer of 321 ASS, treated samples were

Table 1
Chemical composition (wt.%) of 321 ASS.

C	Si	Mn	P	S	Cr	Mo	Ni	Ti	Fe
0.021	0.557	1.485	0.016	0.011	18.104	0.113	9.697	0.461	Bal.

vacuum annealed (10^{-5} mbar) at 200, 400, 600, 800 and 1000 °C for 10 h. The GI-XRD studies were carried out using a X'Pert Pro MPD X-ray diffraction instrument. A scan mode at scan step size of 0.02° (2θ) was used to collect XRD spectra at grazing angle of 2°, using Cu-K$_\alpha$ radiation under 40 kV voltage and 40 mA current. The GI-XRD tests were repeated three times for each sample to ensure the reproducibility. The volume fraction of strain induced martensite (α′) phase was also calculated using the following formula [17]:

$$V_{\alpha'} = \frac{(1/n)\sum_{j=1}^{n}\left(\frac{I_{\alpha'}^{j}}{R_{\alpha'}^{j}}\right)}{(1/n)\sum_{j=1}^{n}\left(\frac{I_{\gamma}^{j}}{R_{\gamma}^{j}}\right) + (1/n)\sum_{j=1}^{n}\left(\frac{I_{\alpha'}^{j}}{R_{\alpha'}^{j}}\right)} \tag{1}$$

where n, I and R are the number of peaks of the phase used in the calculation, the integrated intensity of the reflecting planes and the material scattering factor, respectively. For Eq. (1), only two phases (γ-austenite and α′- strain induced martensite) were considered. The microstrain in the surface layer was evaluated using the Voigt function [18]. The relationship of integral breadth is shown in Eq. (2). The microstrain, ε, can be calculated via Eq. (3).

$$\beta_C^h = \beta_C^f + \beta_C^g; \left(\beta_G^h\right)^2 = \left(\beta_G^f\right)^2 + \left(\beta_G^g\right)^2 \tag{2}$$
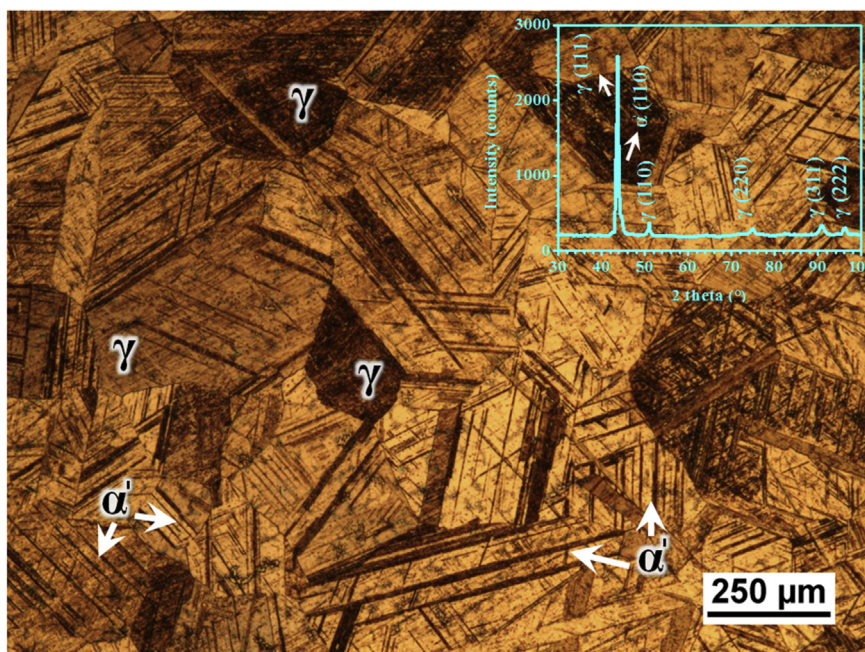
$$\varepsilon = \frac{\beta_G^f}{4\tan\theta} \tag{3}$$

where the subscripts G and C denote the Gaussian and Cauchy components and superscripts h, f, g denote the measured line profile, the structural broadened profile and the instrumental profile in the line profile; β and θ represent the integral breadth and Bragg angle, respectively.

TEM observations at the topmost surface of treated and annealed samples were carried out using a Tecnai G2 operating at 200 kV. TEM foils of the surface layer of treated and annealed

Fig. 1. Optical metallographic view showing γ grains and fine α′ needles. Corresponding XRD pattern shown as inset.

samples were prepared by mechanically grinding of samples from the non-treated side to obtain thin foils with a thickness of ≈ 50 μm. Afterwards, the prepared foils were perforated by dimpling and finally ion-milled on the non-treated side until a thin section with a thickness between tens of nanometers to hundreds of nanometers was achieved. To determine the grain size, at least four dark-field TEM images were processed in microstructural image processing (MIP) software and after that the mean grain size was reported. The overall error associated with the grain size measurements is due to inaccuracies in delineating the grain boundaries as a result of contrast variations. Based on the D and ε values, dislocation density (ρ_d) was calculated by using Eq. (4) [19].

$$\rho_d = \frac{2\sqrt{3}\varepsilon}{Db} \tag{4}$$

where b is the Burgers vector.

Microhardness measurements (≈ 10 μm below the top surface) were done by a Buehler microhardness tester at a load of 20 g and dwell time of 10 s.

3. Results and discussion

3.1. Microstructure characteristics in the initial and treated 321 ASS samples

Microstructure characteristics of the as-received 321 ASS and the surface treated one were reported in detail elsewhere [16]. Specifically, Fig. 1 shows the microstructure characteristics of as-received 321 ASS. As can be seen, the microstructure is composed of two phases: γ grains with an average grain size of ≈ 380 μm and fine needles of α' ($V_{i,\alpha'} \approx 10\%$). After SSP, a considerable amount of γ phase (ICDD 00-033-0397) in the top surface was transformed to α' phase (ICDD 00-035-1375) and $V_{\alpha'}$ increased to 65%. In addition, γ grains were refined to ≈ 75 nm and the dislocation density increased to $\approx 1.11 \times 10^{14}$ m^{-2} in the grains. As a result of severe grain refinement and enhanced formation of α' phase, microhardness in the surface layers of treated 321 ASS increased from ≈ 120 HV (solution-annealed condition) to ≈ 275 HV.

3.2. GI-XRD analyses of the treated-annealed 321 ASS samples

Fig. 2 shows the XRD patterns of treated and treated-annealed 321 ASS samples. As can be seen, peak broadening is completely clear for the as-treated sample which is primarily attributed to the grain refinement and an increase in microstrain after SSP [20]. Following annealing at 200, 400 and 600 °C, the peak broadening is gradually decreased but it is still obvious. With increasing the annealing temperature to 800 and 1000 °C, a considerable narrowing in diffraction peaks is observed, revealing abnormal grain growth and/or strain relaxation at these temperatures. In line with peak narrowing during annealing, α' → γ phase transformation also occurs. As can be seen from Fig. 3, $V_{\alpha'}$ at 200 °C practically remained unchanged compared with the as-treated one; however, its values start to decrease from 400 °C. A sharp decrease in $V_{\alpha'}$ can be seen around 600 °C (Fig. 3), so that this value reaches $\approx 36\%$. Considering XRD resolution, no α' phase was detected at 800 and 1000 °C. This means that even the initial α' martensite which was in the as-received material (Fig. 1, $V_{i,\alpha'} \approx 10\%$) has been transformed to γ. As supported by these results, it can be stated that this transformation is essentially thermally activated (diffusion controlled). This argument is in full agreement with [10].
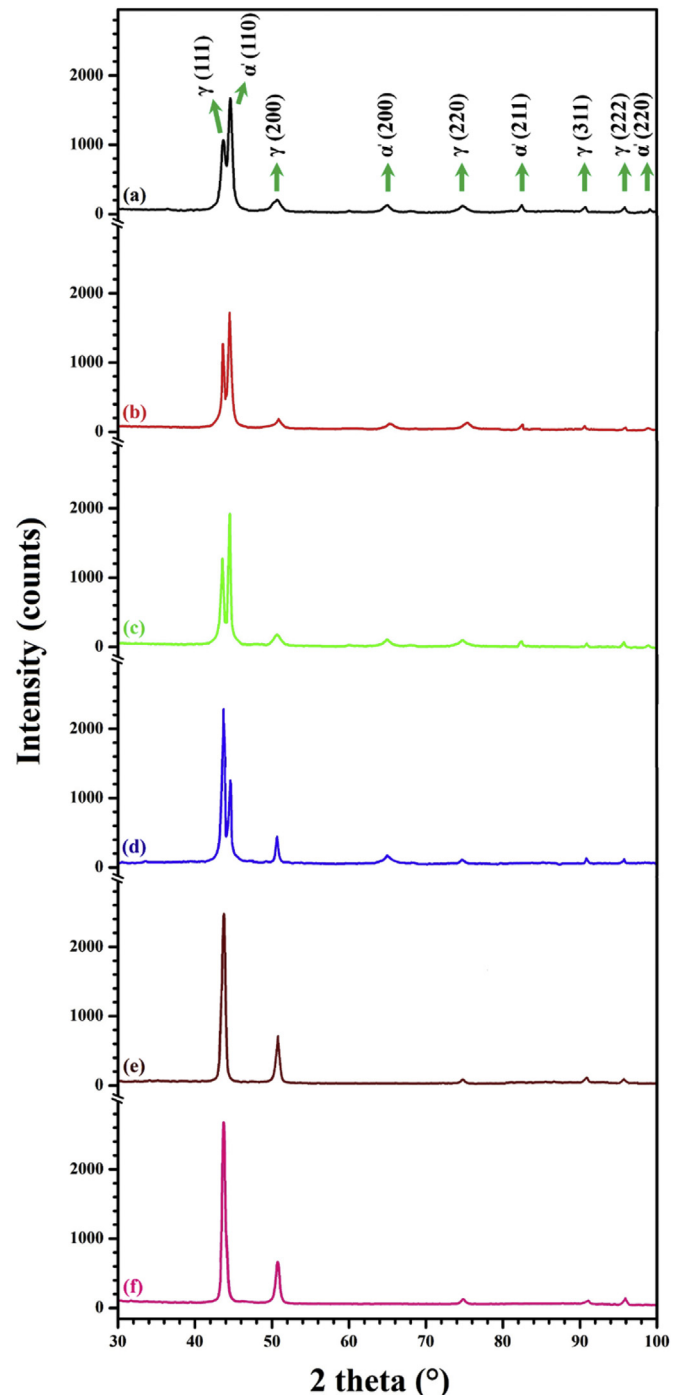

Fig. 2. XRD patterns of 321 ASS after (a) SSP and SSP-annealing at different temperatures (b) 200 °C, (c) 400 °C, (d) 600 °C, (e) 800 °C and (f) 1000 °C.

3.3. Microstructural characteristics of the nanocrystalline surface after annealing

Fig. 4 represents the bright-field TEM images from the topmost surface of as-treated and treated-annealed 321 ASS samples, in which the insets are the corresponding SAED patterns. As can be seen from Fig. 4a, a nearly full surface nanocrystallization is obtained in the case of as-treated sample so that equiaxed nanograins with random crystallographic orientation and a mean size of 75 nm are observed in the whole microstructure. This microstructural refinement is also reflected in the SAED pattern shown as inset in
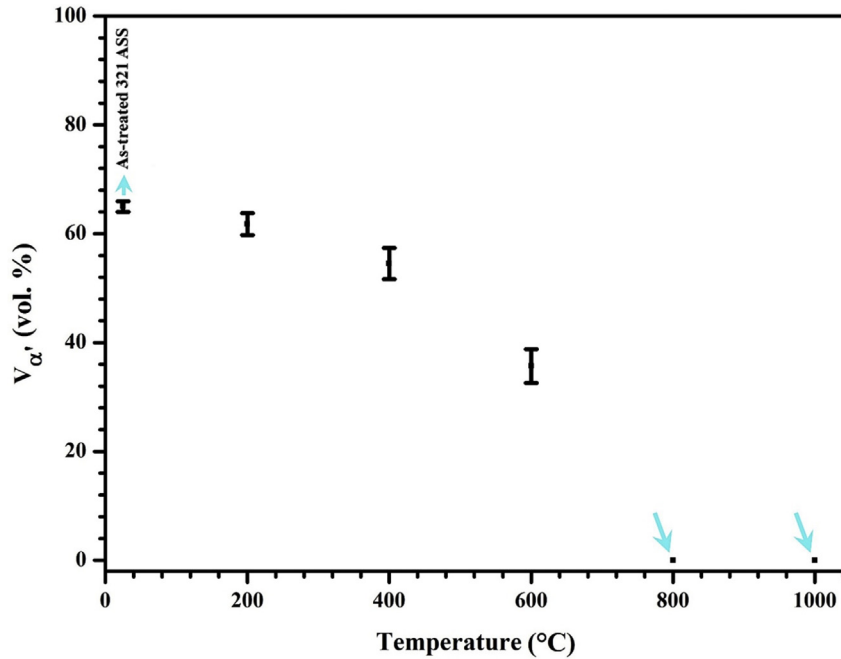
**Fig. 3.** Amount of α′ phase ($V_{α'}$) measured by XRD, as a function of annealing temperature.

Fig. 4a where continuous rings appeared. After annealing at 200 °C, the grain size remains in the range of nanoscale (≈ 96 nm); however, most of the equiaxed nanograins show blurred GBs. This feature after annealing at 200 °C indicates the occurrence of gradual strain relaxation and dislocation annihilation in nanograin boundaries, as has been similarly reported in previous works [21,22]. During the mentioned phenomenon, some areas with dense dislocation tangles are also created (Fig. 4b). In the case of annealing at 400 °C, no nanograins are observed; however, large dislocation tangles, which can be a result of interactions between dissociated nanograin boundaries, are distributed in the whole microstructure. The tangles are tightly stacked behind the GBs. These GBs show a curved morphology, implying the occurrence of thermally activated curvature-driven GBs migration [23]. As can be seen from the SAED pattern (inset of Fig. 4c), streak points instead of continuous rings are apparent, this in turn indicating classical grain growth [24]. With increasing the temperature to 600 °C, the amount of dislocation tangles, i.e. dislocation density, decreases as a result of dislocation annihilation and dislocation absorption by GBs. Dong et al. [25] reported similar arguments for ultrafine grained low carbon steel. At annealing temperatures higher than 600 °C, grain growth is largely enhanced so that ultrafine grains with a recognizable contrast and 13°–17° misorientation are observed in the whole microstructure. Some areas near to the GBs and triple points show spaced traces of dislocations at 800 °C (Fig. 4e) which can provide an indication of dislocation absorption by GBs and triple points. Formation of a dense array of dislocations, similar to dislocation walls inside the grains, is another feature at this temperature. As can be seen from Fig. 4f, a nearly complete recovery with a very low density of dislocations is obtained for annealing at 1000 °C. Compared with Fig. 4a, SAED patterns for latter temperatures also reveal grain growth from nanograins to ultrafine ones. In line with the XRD results, corresponding SAED patterns at 800 and 1000 °C confirm nearly perfect γ crystals distributed in the microstructure, i.e. a complete transformation of the α′ phase to the γ phase has occurred.

Fig. 5 shows the evolution of the grain size and the dislocation density during annealing up to 1000 °C. As can be seen, mean grain

size linearly increases from 75 nm to 411 nm with increasing annealing temperature from room temperature to 600 °C. In this temperature range, dislocation density decreases from $\approx 1.1 \times 10^{14}$ m^{-2} to $\approx 8.7 \times 10^{12}$ m^{-2}. The good thermal stability of nanocrystalline top surface layer in ASS can be due to the high melting point of ≈ 1700 K [26]. Above 600 °C, due to enhanced dislocation annihilation, more absorption of dislocations by GBs and triple points and higher grain growth rate, an unexpected drop and sudden increment is observed for dislocation density and grain size, respectively. It is worthy to note that the α′ → γ phase transformation is accompanied by a volume contraction which may yield internal stresses and formation of lattice defects [27]. So, it can be claimed that the maximum annihilation and absorption of dislocations occur at temperatures between 600 and 800 °C. A nearly unchanged dislocation density is seen for the temperature range of 800–1000 °C, which in turn shows that the growth of ultrafine grains and an increase in their misorientations are the main features in this temperature interval.

Fig. 6 generalizes the physical mechanism of grain structure evolution of nanocrystalline surface layer of 321 ASS subjected to a wide range of temperature from 200 °C to 1000 °C (based on Figs. 4 and 5). For the sake of convenience, only the microstructural evolution of nanograins has been taken into account. As can be seen, nanograin growth probably occurs in the following sequence:

(i) In the first phase (≈ 200 °C), the imparted heat energy is reflected in the GBs dissociation by emission of dislocations as well as by dislocation annihilation. Rittner et al. [28] and Clarebrough et al. [29] also reported that emission of crystallographic defects (low angle GBs, twins, stacking faults, dislocations and etc.) from GBs is a probable way for relaxation during annealing of FCC metals. As a result of this phenomena, nanograin boundaries are not as sharp as those in the as-treated material (Fig. 4b and Fig. 6b).

(ii) In the second phase (≈ 400 °C), increase of input heat energy results in more GBs dissociation and dislocation annihilation, so that nanograins completely are dissociated to dense dislocation tangles with curved boundaries. Latter
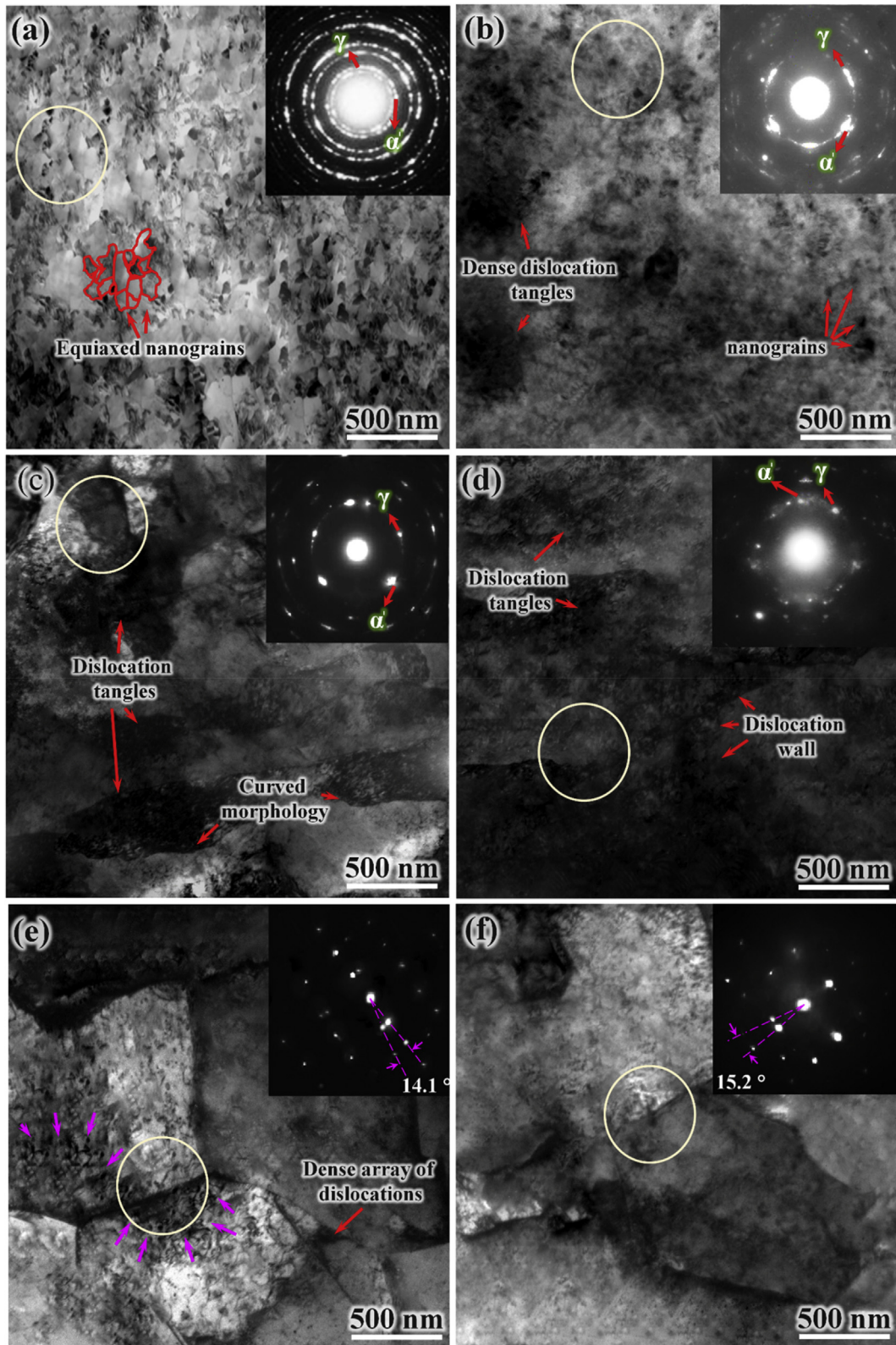
Fig. 4. Bright field TEM images and corresponding SAED patterns (insets) of the nanocrystalline surface layer of 321 ASS (a) after SSP and SSP-annealing at different temperatures: 200 °C, (c) 400 °C, (d) 600 °C, (e) 800 °C and (f) 1000 °C.
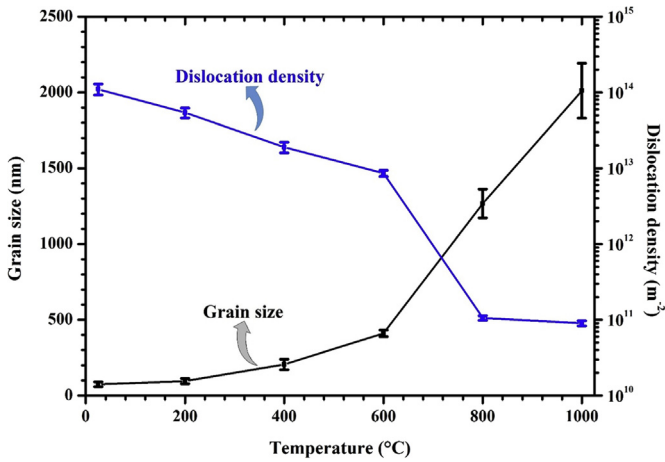
Fig. 5. Evolution of grain size and dislocation density of nanocrystalline surface layer of 321 ASS as a function of annealing temperature.

morphology significantly promotes the transfer of atoms to and from grains which are adjacent to the GBs [30] (Fig. 6c).

(iii) A further increase in temperature results in more dislocation annihilation and their adsorption by GBs. Under these conditions, dislocation walls are formed inside the grains, as can be seen in Fig. 4d and Fig. 6d (third phase: ≈ 600 °C).

(iv) In the fourth phase (≈ 800 and 1000 °C), ultrafine recrystallized grains with middle angle boundaries (misorientation angle between 13° and 17°) are formed in the whole microstructure. Due to the high rate of dislocation annihilation and their absorption by GBs, dislocation density severely drops at such high temperatures (Fig. 4e, f, Fig. 5 and Fig. 6f).

3.4. Microhardness variation after annealing

Fig. 7 shows the variation of microhardness in the nanocrystalline surface layer of 321 ASS after SSP and SSP-annealing. The microhardness of the nanocrystalline layer is about 281 HV, which
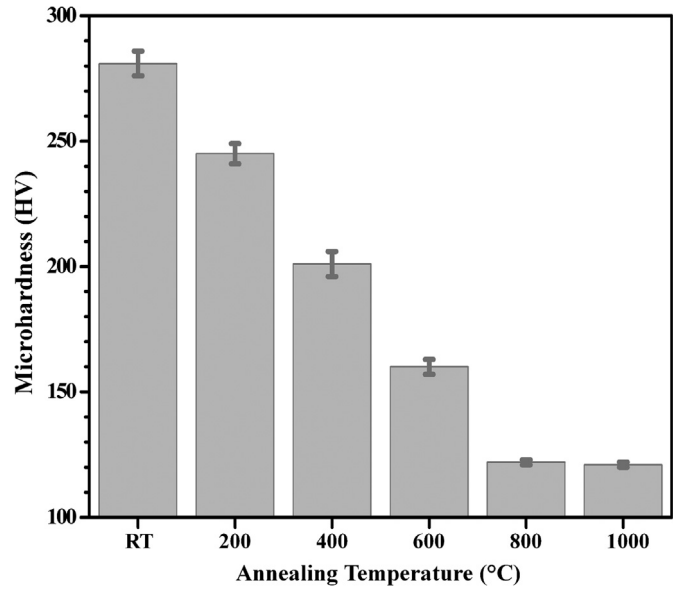

Fig. 7. Microhardness values of nanocrystalline surface layer of 321 ASS at different temperatures (RT: room temperature).

is more than two times larger than that of as-received 321 ASS. In terms of the Hall-Petch relationship, this increase is mainly attributed to the presence of nanograins [16]. Moreover, it can also be seen that the microhardness values continuously decrease with increasing the annealing temperature to reach 800 °C and after that, they remain almost constant. Comparing the microstructural features (especially grain size and dislocation density), phase fractions and microhardness values obtained for different temperatures in Figs. 3–5 and 7, it appears that the microhardness evolution during annealing is mostly determined by the dislocation density. Colaco et al. [31], based on Nix-Gao model, also reported that the microhardness of ultrafine grained FCC metals is directly related to their dislocation density.
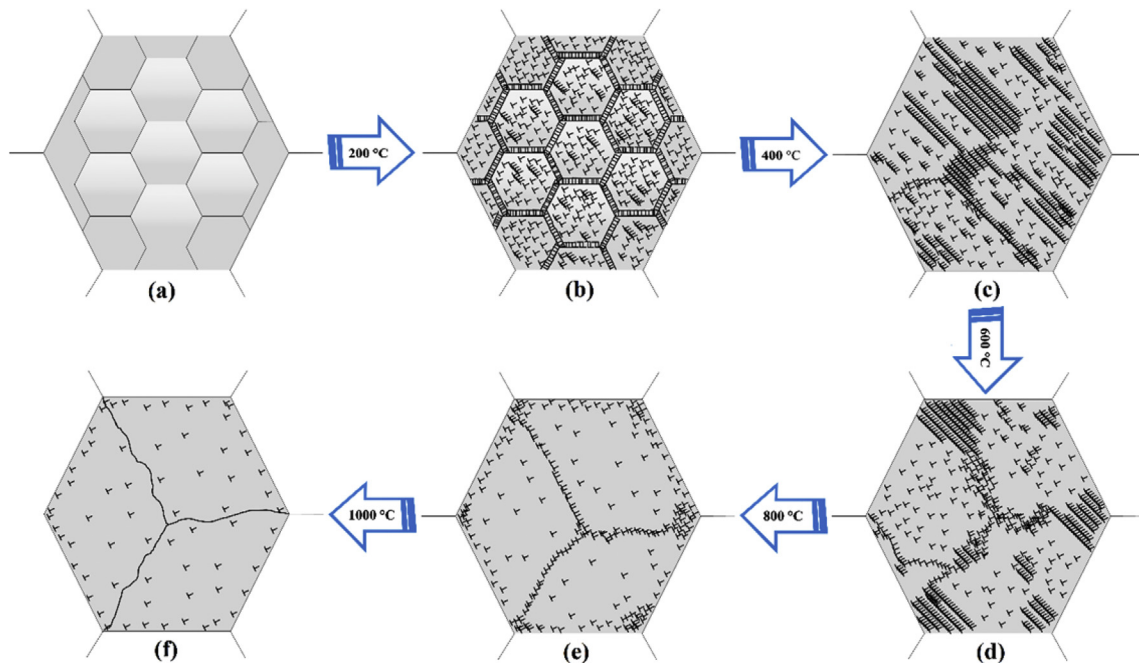

Fig. 6. Schematic diagram of physical mechanism of growth of nanograins after annealing at different temperatures.

4. Conclusions

TEM and GI-XRD were applied to investigate the microstructural evolution of nanocrystalline surface layer of 321 ASS in the temperature range of 200–1000 °C. The main results are summarized as follows:

(1) At 200 °C: nanograined structure remains stable for 10 h of annealing. However, nanograin boundaries start to dissociate by emission of dislocations.
(2) At 400 °C: due to dislocation annihilation and growth of nanograins, large dislocation tangles and no nanograins are observed in the whole microstructure. In addition, $V_{\alpha'}$ starts to decrease and reach 55%.
(3) At 600 °C: density of dislocations is decreased so that the dislocation walls are formed inside the γ grains instead of dense dislocation tangles. $V_{\alpha'}$ values also decrease to 36%.
(4) At 800 and 1000 °C: middle angle boundaries (between 13° and 17°) are formed and stable ultrafine grains are distributed in the whole microstructure. Due to enhanced dislocation annihilation and absorption of dislocations by grain boundaries and triple points, the density of dislocations severely decreased at 800 °C temperature. Complete $\alpha' \rightarrow \gamma$ phase transformation takes place at temperatures higher than 800 °C.
(5) In line with the considerable decrease in dislocation density from room temperature ($\approx 1.10 \times 10^{14}$ m^{-2}) to 800 °C ($\approx 1.06 \times 10^{11}$ m^{-2}), microhardness values also decrease from 281 HV to 122 HV. At 1000 °C, these two parameters are comparable with those of 800 °C.

Acknowledgements

References

[1] M.F. McGuire, Stainless Steels for Design Engineers, Asm International, 2008.
[2] S. Kumar, K. Chattopadhyay, V. Singh, Effect of surface nanostructuring on corrosion behavior of Ti–6Al–4V alloy, Mater. Charact. 121 (2016) 23–30, https://doi.org/10.1016/j.matchar.2016.09.031.
[3] Y. Lin, J. Lu, L. Wang, T. Xu, Q. Xue, Surface nanocrystallization by surface mechanical attrition treatment and its effect on structure and properties of plasma nitrided AISI 321 stainless steel, Acta Mater 54 (2006) 5599–5605, https://doi.org/10.1016/j.actamat.2006.08.014.
[4] X. Peng, J. Yan, Y. Zhou, F. Wang, Effect of grain refinement on the resistance of 304 stainless steel to breakaway oxidation in wet air, Acta Mater 53 (2005) 5079–5088, https://doi.org/10.1016/j.actamat.2005.07.019.
[5] S.G. Wang, M. Sun, H.B. Han, K. Long, Z.D. Zhang, The high-temperature oxidation of bulk nanocrystalline 304 stainless steel in air, Corros. Sci. 72 (2013) 64–72, https://doi.org/10.1016/j.corsci.2013.03.008.
[6] L. Pantělejev, R. Štěpánek, O. Man, Thermal stability of bimodal microstructure in magnesium alloy AZ91 processed by ECAP, Mater. Charact. 107 (2015) 167–173, https://doi.org/10.1016/j.matchar.2015.07.009.
[7] K. Abib, H. Azzeddine, K. Tirsatine, T. Baudin, A.-L. Helbert, F. Brisset, B. Alili, D. Bradai, Thermal stability of Cu-Cr-Zr alloy processed by equal-channel angular pressing, Mater. Charact. 118 (2016) 527–534, https://doi.org/10.1016/j.matchar.2016.07.006.
[8] W. Jia, H. Zhao, Q. Hong, L. Li, X. Mao, Research on the thermal stability of a near α titanium alloy before and after laser shock peening, Mater. Charact. 117 (2016) 30–34, https://doi.org/10.1016/j.matchar.2016.04.019.
[9] A.R. Kalidindi, C.A. Schuh, Stability criteria for nanocrystalline alloys, Acta Mater 132 (2017) 128–137, https://doi.org/10.1016/j.actamat.2017.03.029.
[10] M. El-Tahawy, Y. Huang, H. Choi, H. Choe, J.L. Lábár, T.G. Langdon, J. Gubicza, High temperature thermal stability of nanocrystalline 316L stainless steel processed by high-pressure torsion, Mater. Sci. Eng. A 682 (2017) 323–331, https://doi.org/10.1016/j.msea.2016.11.066.
[11] T. Chookajorn, H.A. Murdoch, C.A. Schuh, Design of stable nanocrystalline alloys, Science 337 (2012) 951–954 (80-.).
[12] M. Ames, J. Markmann, R. Karos, A. Michels, A. Tschöpe, R. Birringer, Unraveling the nature of room temperature grain growth in nanocrystalline materials, Acta Mater 56 (2008) 4255–4266, https://doi.org/10.1016/j.actamat.2008.04.051.
[13] L. Zábranský, V. Buršíková, P. Souček, P. Vašina, J. Dugáček, P. Sťahel, J. Buršík, M. Svoboda, V. Peřina, Thermal stability of hard nanocomposite Mo-B-C coatings, Vacuum 138 (2017) 199–204, https://doi.org/10.1016/j.vacuum.2016.12.016.
[14] Y. Mai, X. Jie, L. Liu, N. Yu, X. Zheng, Thermal stability of nanocrystalline layers fabricated by surface nanocrystallization, Appl. Surf. Sci. 256 (2010) 1972–1975, https://doi.org/10.1016/j.apsusc.2009.09.030.
[15] L. Hultman, Thermal stability of nitride thin films, Vacuum 57 (2000) 1–30, https://doi.org/10.1016/S0042-207X(00)00143-3.
[16] S. Pour-Ali, A.-R. Kiani-Rashid, A. Babakhani, Surface nanocrystallization and gradient microstructural evolutions in the surface layers of 321 stainless steel alloy treated via severe shot peening, Vacuum 144 (2017) 152–159, https://doi.org/10.1016/j.vacuum.2017.07.016.
[17] A.K. De, D.C. Murdock, M.C. Mataya, J.G. Speer, D.K. Matlock, Quantitative measurement of deformation-induced martensite in 304 stainless steel by X-ray diffraction, Scr. Mater 50 (2004) 1445–1449, https://doi.org/10.1016/j.scriptamat.2004.03.011.
[18] T.H. De Keijser, J.I. Langford, E.J. Mittemeijer, A.B.P. Vogels, Use of the Voigt function in a single-line method for the analysis of X-ray diffraction line broadening, J. Appl. Crystallogr. 15 (1982) 308–314.
[19] R. Wang, Z. Zheng, Q. Zhou, Y. Gao, Effect of surface nanocrystallization on the sensitization and desensitization behavior of Super304H stainless steel, Corros. Sci. 111 (2016) 728–741, https://doi.org/10.1016/j.corsci.2016.06.012.
[20] S. Pour-Ali, A. Kiani-Rashid, A. Babakhani, A. Davoodi, Enhanced protective properties of epoxy/polyaniline-camphorsulfonate nanocomposite coating on an ultrafine-grained metallic surface, Appl. Surf. Sci. 376 (2016) 121–132, https://doi.org/10.1016/j.apsusc.2016.03.131.
[21] R. Huang, Y. Han, Structure evolution and thermal stability of SMAT-derived nanograined layer on Ti–25Nb–3Mo–3Zr–2Sn alloy at elevated temperatures, J. Alloys Compd. 554 (2013) 1–11, https://doi.org/10.1016/j.jallcom.2012.09.045.
[22] W. Chen, Q. Sun, L. Xiao, J. Sun, Thermal stability of bulk nanocrystalline Ti–10V–2Fe–3Al alloy, Mater. Sci. Eng. A 536 (2012) 223–230, https://doi.org/10.1016/j.msea.2012.01.001.
[23] F.J. Humphreys, M. Hatherly, Recrystallization and Related Annealing Phenomena, Elsevier, 2012.
[24] C. Mangler, C. Gammer, H.P. Karnthaler, C. Rentenberger, Structural modifications during heating of bulk nanocrystalline FeAl produced by high-pressure torsion, Acta Mater 58 (2010) 5631–5638, https://doi.org/10.1016/j.actamat.2010.06.036.
[25] K.-T. Park, Y.-S. Kim, J.G. Lee, D.H. Shin, Thermal stability and mechanical properties of ultrafine grained low carbon steel, Mater. Sci. Eng. A 293 (2000) 165–172, https://doi.org/10.1016/S0921-5093(00)01220-X.
[26] L. Sun, K. Muszka, B.P. Wynne, E.J. Palmiere, On the interactions between strain path reversal and dynamic recrystallisation in 316L stainless steel studied by hottorsion, Mater. Sci. Eng. A 568 (2013) 160–170, https://doi.org/10.1016/j.msea.2013.01.045.
[27] E. Dryzek, M. Sarnek, M. Wróbel, Reverse transformation of deformation-induced martensite in austenitic stainless steel studied by positron annihilation, J. Mater. Sci. 49 (2014) 8449–8458.
[28] J.D. Rittner, D.N. Seidman, K.L. Merkle, Grain-boundary dissociation by the emission of stacking faults, Phys. Rev. B 53 (1996) R4241.
[29] L.M. Clarebrough, C.T. Forwood, The properties of a near $\sum$ 9 grain boundary. III. Boundary dissociation, Phys. Status Solidi 60 (1980) 51–57.
[30] L. Li, M.Q. Li, Thermal stability and microstructure evolution in nanocrystalline Ti-5Al-2Sn-2Zr-4Mo-4Cr – A HRTEM study, J. Alloys Compd. 715 (2017) 112–121, https://doi.org/10.1016/j.jallcom.2017.04.303.
[31] S. Graça, R. Colaço, P.A. Carvalho, R. Vilar, Determination of dislocation density from hardness measurements in metals, Mater. Lett. 62 (2008) 3812–3814, https://doi.org/10.1016/j.matlet.2008.04.072.